* Text only

Anisotropic Elastic Constants and Thermal Expansivities in Monocrystal CrB_2, TiB_2, and ZrB_2

By Norihiko L. Okamoto,[1,*] Misato Kusakari,[1] Katsushi Tanaka,[1] Haruyuki Inui[1] and Shigeki Otani[2]

[1]Department of Materials Science and Engineering, Kyoto University

Sakyo-ku, Kyoto 606-8501, Japan

[2]Advanced Materials Laboratory, National Institute for Materials Science

1-1, Namiki, Tsukuba, Ibaraki 305-0044, Japan

Abstract

The elastic constants and thermal expansivities in monocrystals of three transition-metal diborides with the AlB_2 structure, CrB_2, TiB_2 and ZrB_2 have been investigated in the temperature range from 300 to 1373K and from 300 to 1073K, respectively. The anisotropic parameters deduced from the measured elastic constants and thermal expansivities indicate that of the three diborides, the anisotropy is the most and least significant in CrB_2 and ZrB_2, respectively. The factors determining the significance in anisotropy in atomic bonding in AlB_2-type diborides are analyzed by an approach similar to the valence-force-field method and are discussed in terms of the deformation of the electronic charge around the metal atoms occurring to fit themselves in the (0001) basal plane.

Keywords: Borides; Transition-metals; Monocrystals; Anisotropy; High temperatures

***Corresponding Author Contact Information:**

Norihiko L. Okamoto

Department of Materials Science and Engineering, Kyoto University

Sakyo-ku, Kyoto 606-8501, Japan

Phone: +81-75-753-5481

Fax: +81-75-753-5461

E-mail: n.okamoto@at4.ecs.kyoto-u.ac.jp

1. Introduction

Many transition-metal diborides, MB_2 (M: transition-metal atom) with the hexagonal AlB_2 structure (space group: *P*6/mmm) exhibit a wide variety of attractive properties such as high melting temperature, high stiffness and hardness, and high electrical and thermal conductivity [1-3] and thus have many different applications. For example, TiB_2 has often been used as reinforcements in various composite materials such as steel [4]. TiB_2 has also been considered in applications in diffusion barriers for preventing electromigration in very large-scale integrated (LSI) circuits because of the very low diffusion coefficient [5]. ZrB_2 and HfB_2 have long been used as refractory crucibles and sheaths in steel making industries because of their high corrosion-resistance [6]. In addition, ZrB_2 is recently under consideration for the use as a substrate for heteroepitaxial growth of GaN because of small mismatches in lattice constants and thermal expansivities with GaN [7-12].

The hexagonal AlB_2 structure, into which these transition-metal diborides crystallize, is build up of hexagonal nets of pure transition-metal atoms and triangle nets of pure boron atoms, which are alternately stacked along the *c*-axis, as shown in Fig. 1. The crystal structure can hence be regarded as a layered structure. If we describe the crystal structure as a packing of touching spheres with R_M and R_B (radii of M and B atoms), simple geometrical consideration gives the M-M distance ($=2R_M$) as a, the B-B distance ($=2R_B$) as $a/3^{1/2}$ and the M-B distance ($=R_M + R_B$) as $(a^2/3 + c^2/4)^{1/2}$, where a and c denote the lattice constants along the *a*- and *c*- axes, respectively. Hence, the ideal c/a axial ratio of 1.0746 ($=(4/3)^{1/4}$) is deduced together with the ideal atomic size ratio $R_M/R_B = 3^{1/2} = 1.732$. In fact, c/a axial ratios for many transition-metal diborides are close to the above ideal value as shown in the left-hand side of Fig. 2 [13] while those for lanthanoid-metal diborides are larger than the ideal value as shown in the right-hand side of the figure. Close examination of the c/a axial ratios indicates that the c/a axial ratios of some diborides formed with, for example, Cr, V and

Ta are a little smaller than the ideal value, while those of other diborides formed with, for example, Hf, Zr and most of lanthanoid-metals are a little larger than the ideal one, and that diborides formed with Al, Ti and Nb possess the *c*/*a* axial ratios very close to the ideal value. When considering the fact that the crystal structure can be regarded as a layered structure, physical properties are expected to be highly anisotropic and the extent of the anisotropy varies from diboride to diboride, depending on their *c*/*a* axial ratios. However, because mainly of the inherent difficulty in growing monocrystals of transition-metal diborides due to their high melting points (usually exceeding 2500 K, see Table 1) [14-16], almost nothing is known about how their physical properties vary with crystallographic directions (anisotropy) and how the extent of anisotropy varies from diboride to diboride for most of these transition-metal diborides.

In the present study, we investigate monocrystal elastic constants and thermal expansivities as a function of crystal orientation with the use of monocrystals of CrB_2, TiB_2 and ZrB_2, whose *c*/*a* axial ratios are smaller than, almost identical with and larger than the ideal value, respectively, as shown in Fig. 2 and Table 1. We discuss anisotropy in physical properties of these transition-metal diborides in terms of chemical bondings.

2. Experimental procedures

Monocrystals of CrB_2 were grown with an optical floating-zone furnace while those of TiB_2 and ZrB_2 were grown with a radio-frequency (RF) heated floating-zone furnace as described previously [17, 18]. After determining the crystallographic orientations by the X-ray back reflection Laue method, specimens with a rectangular parallelepiped shape having three orthogonal faces parallel to the (0001), $(11\bar{2}0)$ and $(1\bar{1}00)$ planes were cut from the crystals by spark-machining. Then, the specimen surface was mechanically polished with diamond paste. The maximum error in parallelism for each face was at most 3 μm/mm. The

deviation from the respective crystallographic orientation was smaller than 0.2° for each face. The dimensions of specimens used for the measurements of elastic constants and thermal expansivities are summarized in Table 2.

Measurements of elastic constants were carried out by the rectangular parallelepiped resonance (RPR) method [19] in the temperature range from room temperature to 1373K. In this method, all elastic constants are derived from the frequencies of resonance vibrations of specimen [19]. Measurements of thermal expansivities were carried out with a push-rod type differential dilatometer (Shimazdu TMA-60) in the temperature range from room temperature to 1073 K at the heating rate of 5 K per minute under an Ar gas flow.

3. Results

3.1. Monocrystal elastic constants

Monocrystal elastic constants of CrB_2, TiB_2 and ZrB_2 are plotted respectively in Figs. 3(a)-(c) as a function of temperature. Values of c_{11}, c_{33} and c_{44} decrease monotonically with the increase in temperature, while those of c_{12} and c_{13} are virtually temperature independent for all transition-metal diborides investigated. Although actual temperature dependence of elastic constants is slightly nonlinear even in very-well-behaved materials, these data points for each of the five elastic constants are fitted to a linear equation in the form of

$$c_{ij} = c_{ij(300K)} + k(T - 300), \qquad (1)$$

where $c_{ij(300K)}$, k and T stand respectively for the elastic constant at 300 K, numerical constant and temperature in Kelvin, as tabulated in Table 3. The values of elastic constants for TiB_2 determined in the present study agree well with those previously reported by Spoor et al. [20] but not completely with those reported by Gilman et al. [21]. In particular, the values of c_{12} and c_{13} determined in the present study are considerably smaller than those reported by Gilman et al. [21]. While the values of c_{12} and c_{13} for CrB_2 are comparable to that of c_{44}, those

of c_{12} and c_{13} for TiB_2 and ZrB_2 are notably smaller than those of the other constants, indicating the brittleness of TiB_2 and ZrB_2. The values of anisotropic parameters defined in crystals with the hexagonal symmetry as c_{33}/c_{11} and c_{44}/c_{66} are both the largest for ZrB_2 and the smallest for CrB_2, as tabulated in Table 3.

The orientation dependence of Young modulus on $(1\bar{1}00)$ prism plane at 300 and 1373 K is depicted in Fig. 4(a) for CrB_2, TiB_2 and ZrB_2. The curves in Fig. 4(a) are calculated with the following equation [22]:

$$1/E = s_{11} \cdot sin^4\theta + s_{33} \cdot cos^4\theta + (s_{44} + 2s_{13}) sin^2\theta \cdot cos^2\theta , \quad (2)$$

where θ is the angle between the corresponding loading direction and the *c*-axis, *E* is Young modulus along the loading direction, and s_{ij} is elastic compliance constants. The values of Young modulus increase monotonically as the angle θ increases for CrB_2 and TiB_2, whereas those for ZrB_2 exhibit a maximum along a direction approximately θ=60° at both 300 and 1373 K. The values of Young modulus along the *a*- (E_a) and *c*-axes (E_c) at 300 K as well as their ratio (E_c/E_a) are tabulated in Table 4 for CrB_2, TiB_2 and ZrB_2. The value of E_c/E_a increases in the order of CrB_2, TiB_2 and ZrB_2. The values of E_a and E_c are both the largest for TiB_2 and the smallest for CrB_2, but the value of E_c/E_a is the largest for ZrB_2 and the smallest for CrB_2.

Linear compressibilities along the *a*- and *c*-axes, β_a and β_c, for a hexagonal crystal can be defined with the following equations [22];

$$\beta_a = s_{11} + s_{12} + s_{13} , \quad (3)$$

$$\beta_c = 2s_{13} + s_{33} . \quad (4)$$

The reciprocal values of β_a and β_c and their ratio at 300 K are tabulated in Table 4 for CrB_2, TiB_2 and ZrB_2. The value of β_a^{-1} is the largest for CrB_2 and is the smallest for ZrB_2, but that of β_c^{-1} is the largest for ZrB_2 and is the smallest for CrB_2. The value of $\beta_c^{-1}/\beta_a^{-1}$ is the largest for ZrB_2 and the smallest for CrB_2.

3.2. Polycystalline elastic moduli

Polycrystalline elastic moduli are evaluated from the monocrystal elastic constants by the Hill's method [23]. The temperature dependence of Young (*E*), bulk (*B*) and shear (*G*) moduli as well as that of Poisson ratio are illustrated in Figs. 5(a)-(c) respectively for CrB_2, TiB_2 and ZrB_2. As in the case of monocrystal elastic constants, the values of Young, bulk and shear moduli all decrease monotonically with increasing temperature. While the values of shear modulus are comparable with those of bulk modulus for TiB_2 and ZrB_2, those of shear modulus are smaller than those of Young and bulk moduli for CrB_2. This is because of the exceptionally small values of c_{44} for CrB_2 as shown in Fig. 3(a). Although the bulk moduli of the pure transition metals differ considerably [Cr: 190; Ti: 105; Zr: 83 (GPa)] [24], those of the boride compounds are similar, indicating the strong role of covalent B-B bonding. The values of Poisson ratio generally increase with increasing temperature and range from 0.206 to 0.230, from 0.112 to 0.123, and from 0.133 to 0.151 for CrB_2, TiB_2 and ZrB_2, respectively. The small values of Possion ratio again indicate the strong covalence in these diborides. The data points for each of these polycrystalline elastic moduli as well as Poisson ratio are fitted to a linear equation in the form of Eq. (1). The values of polycrystalline elastic moduli and Poisson ratio at 300 K are tabulated in Table 5 for CrB_2, TiB_2 and ZrB_2, together with the numerical constants in the fitting equation.

3.3. Thermal expansivities

Thermal expansivity data obtained along the *a*- and *c*-axes as relative elongation with respect to the original specimen length at room temperature were fitted with a quartic function. Thermal expansivities were, then, derived by differentiating the fitted quartic function with respect to temperature. The values of thermal expansivities thus determined are plotted in Figs.

6(a)-(c) as a function of temperature for CrB_2, TiB_2 and ZrB_2, respectively. For CrB_2, the value of thermal expansivity along the *a*-axis (α_a) is as large as 14.0×10^{-6} K^{-1} at room temperature and rapidly decreases with increasing temperature up to around 700K, followed by a slight increase at higher temperatures. On the other hand, the value of thermal expansivity along the *c*-axis (α_c) for CrB_2 is as small as 2.9×10^{-6} K^{-1} at room temperature and monotonically increases with increasing temperature. We consider that the unusual temperature dependence of thermal expansivities for CrB_2 may be related to the magnetic thermal expansion due to the antiferromagnetism of CrB_2 as reported by Nishihara et al. [25]. On the other hand, the temperature dependence of thermal expansivities along the *a*- and *c*-axes for TiB_2 and ZrB_2 is rather small when compared to that for CrB_2. The value of thermal expansivity along the *c*-axis is considerably larger (by almost 50 %) than the corresponding value along the *a*-axis for TiB_2. For ZrB_2, on the other hand, the value of thermal expansivity along the *c*-axis is slightly larger than the corresponding value along the *a*-axis at temperatures below around 700K while they are virtually identical to each other at higher temperatures. The values of thermal expansivities averaged over the temperature range from 300 to 1073 K are tabulated in Table 6, together with the ratio of the thermal expansivities along the *a*- and *c*-axes.

4. Discussion

The anisotropic parameters in elasticity, c_{33}/c_{11}, c_{44}/c_{66}, E_c/E_a and $\beta_c^{-1}/\beta_a^{-1}$ for CrB_2, TiB_2 and ZrB_2 are plotted in Fig. 7 as a function of the magnitude of their *a*-axis lattice constant together with those in thermal expansivity, α_c/α_a. All the anisotropic parameters in elasticity are smaller than unity whereas those of thermal expansivity are larger than unity (except for the α_c/α_a value for CrB_2), indicating that atomic bonding along the *a*-axis is stronger than that along the *c*-axis for all the diborides, which is consistent with the fact that

the AlB_2-type crystal structure is of the layered-type, in which hexagonal nets of pure transition-metal atoms and pure boron atoms stacked alternatively along the *c*-axis. Of the three diborides, the anisotropy is the least significant in ZrB_2 since the values of c_{44}/c_{66} and α_c/α_a are close to unity. This is somewhat surprising when considering the fact that ZrB_2 exhibits the largest value of the c/a axial ratio, since the ratio of the strength of atomic bonding along the *c*-axis to that along the *a*-axis is considered to be the smallest on the rough assumption that the atomic bond strength decreases with the increase in the bond distance. In the following, we will discuss some possible reasons why ZrB_2 with the largest *c*/*a* axial ratio exhibits the least significant anisotropic behavior and vise versa.

If the B-B distance in the (0001) plane of an AlB_2-type metal diboride is assumed to be identical with the covalent bonding distance of B atoms in pure α-boron (0.176 nm) [26], the magnitude of the *a*-axis lattice constant of the diboride should be 0.305 nm since the B-B distance ($=2R_B$) corresponds to $a/3^{1/2}$, as described in Introduction section. On the basis of a packing of touching spheres of M and B atoms in describing the crystal structure, the Goldschmidt radius ($R_{M(G)}$) of the M atom should be 0.152 nm as the M-M distance ($=2R_M$) corresponds to *a*. This value of the Goldschmidt radius ($R_{M(G)}$) for the M atom is designated as the ideal Goldschmidt radius ($R_{M(ideal)}$). In this circumstance, the ideal *c*/*a* axial ratio of 1.0746 ($=(4/3)^{1/4}$) is achieved with the ideal atomic size ratio $R_M/R_B = 3^{1/2}=1.732$. This is almost completely achieved for TiB_2 with the Goldschmidt radius ($R_{Ti(G)}$) of 0.146 nm [27]. However, if the constituent M atom in a metal diboride possesses $R_{M(G)}$ larger than the ideal value ($R_{M(ideal)}$=0.152 nm), the diboride should expand along the *a*-axis in the (0001) plane so as to make the B-B distance larger than 0.176 nm. This corresponds to the case of ZrB_2, in which the B-B distance is 0.1807 nm. However, this expansion along the *a*-axis is not sufficient to allow Zr atoms packed hexagonally in the (0001) plane in ZrB_2 and there still exist the overlapping of Zr atom spheres, as shown in Fig. 8(a). Then, the electronic charge

around Zr atoms in ZrB_2 is considered to deform to elongate along the *c*-axis (Fig. 8(b)). As a result, the interaction along the *c*-axis is expected to become relatively stronger in spite of the *c*/*a* axial ratio (1.129) larger than the ideal one (1.0746). The atomic bonding in ZrB_2 is thus considered to be more isotropic than that in TiB_2.

On the other hand, if the constituent M atom of a metal diboride possesses $R_{M(G)}$ smaller than the ideal value, the diboride should contract along the *a*-axis in the (0001) plane. This corresponds to the case of CrB_2 whose *a*-axis lattice constant (0.2973 nm) [13] is smaller than the ideal one (0.305 nm). This contraction along the *a*-axis for CrB_2 is not sufficient for hexagonally-arranged spheres of Cr atoms to touch each other in the (0001) plane and the Cr atom spheres are left separated in the (0001) plane, as shown in Fig. 8(c). Then, the electronic charge around Cr atoms in CrB_2 is considered to deform to elongate along the *a*-axis (Fig. 8(d)). As a result, the interaction along the *c*-axis is expected to become relatively weaker in spite of the *c*/*a* axial ratio (1.033) smaller than the ideal one (1.0746). The anisotropy in atomic bonding is thus considered to be more significant in CrB_2 than in TiB_2.

The fact that the relative atomic bond strength in basal plane (along the *a*-axis) with respect to that out of basal plane (along the *c*-axis) increases in the order of ZrB_2, TiB_2 and CrB_2 can be quantitatively validated by deriving force constants both in and out of basal plane from their elastic constants. These force constants are analyzed by adopting an approach similar to the valence-force-field method [28-31]. In this approach, all interatomic forces are resolved into bond-stretching and bond-bending forces and the elastic properties are described with the force constants corresponding to these two forces. Because of the strong role of covalent B-B bonding, the bond-bending (non-central) forces in CrB_2, TiB_2 and ZrB_2 are considered to be significant. However, we here consider only the bond-stretching (central) interaction between a given atom and its first-nearest-neighbor atoms in order to deduce the bond-stretching force constants in and out of basal plane from the experimentally determined

elastic constants [32]. If we ignore the bond-bending interaction, the total elastic energy of a metal diboride, U can be written as follows,

$$U = k_a \sum_i (\Delta r_i)^2 + k_c \sum_i (\Delta r_i)^2 \quad , \tag{5}$$

where k_a and k_c are the force constants in and out of basal plane, respectively, and Δr_i is the change in the bond length between the given atom and the ith first-nearest-neighbor atom. The magnitude of Δr_i is calculated for the deformation matrix $\boldsymbol{\varepsilon}$ by the following equation,

$$\Delta r_i = \frac{\mathbf{r}_i \cdot \boldsymbol{\varepsilon} \cdot \mathbf{r}_i^t}{|\mathbf{r}_i|^2} \quad , \tag{6}$$

where $\mathbf{r}_i$ is a position (row) vector for the ith first-nearest-neighbor atom while $\mathbf{r}_i^t$ is the transposed (column) vector of $\mathbf{r}_i$. The elastic constants are derived as the second derivative of Eq. (5) as follows,

$$c_{ij} = \frac{d^2}{d\varepsilon^2} U(\varepsilon) \quad , \tag{7}$$

where ε is the magnitude of strain corresponding to c_{ij}. We will express c_{44} and c_{66} with the force constants, since the change in anisotropy in elastic properties for CrB_2, TiB_2 and ZrB_2 is best described with the c_{44}/c_{66} ratio (Fig. 7) although hexagonal crystals provide anisotropic parameters of c_{13}/c_{12}, c_{33}/c_{11}, $c_{44}/(c_{11}\text{-}c_{12})$ and so forth other than c_{44}/c_{66}. If the following deformation matrices are used,

$$\boldsymbol{\varepsilon}(c_{44}) = \frac{1}{2}\begin{pmatrix} 0 & 0 & 0 \\ 0 & 0 & \varepsilon \\ 0 & \varepsilon & 0 \end{pmatrix}, \quad \boldsymbol{\varepsilon}(c_{66}) = \frac{1}{2}\begin{pmatrix} 0 & \varepsilon & 0 \\ \varepsilon & 0 & 0 \\ 0 & 0 & 0 \end{pmatrix}, \tag{8}$$

the elastic constants c_{44} and c_{66} are deduced with the force constants k_a and k_c as follows,

$$c_{44} = 0k_a + 48\left(\frac{\sqrt{3}(c/a)}{4+(c/a)^2}\right)^2 k_c \,, \tag{9}$$

$$c_{66} = 3k_a + 16\left(\frac{\sqrt{3}}{4+(c/a)^2}\right)^2 k_c \,. \tag{10}$$

The constants of the second term in Eqs. (9) and (10) vary with the c/a axial ratio and the values for CrB_2, TiB_2 and ZrB_2 are tabulated in Table 7. The ratio of k_a/k_c with which the value of c_{44}/c_{66} coincides with the experimentally determined value is tabulated in Table 7. The ratio of k_a/k_c is the largest for CrB_2 and is the smallest for ZrB_2, which is consistent with our qualitative expectation that the ratio of the atomic bond strength in basal plane to that out of basal plane is the largest for CrB_2 and is the smallest for ZrB_2.

The value of $R_{M(G)}$-$R_{M(ideal)}$ is thus considered to be a good indicator for predicting the extent of the anisotropy in atomic bonding in metal diborides with the AlB_2 structure. The values of the anisotropic parameters c_{44}/c_{66} derived by ab-initio calculations by Shein et al. [33] are plotted in Fig. 9 as a function of the value of $R_{M(G)}$-$R_{M(ideal)}$. The experimental values of c_{44}/c_{66} for CrB_2, TiB_2 and ZrB_2 determined in the present study are also plotted with solid circles in the figure. The values of c_{44}/c_{66} for all the metal diborides except for MgB_2 and AlB_2 generally increase with the increase in the value of $R_{M(G)}$-$R_{M(ideal)}$. This is consistent with what is discussed in the present paper in terms of the anisotropy in atomic bonding of AlB_2-type borides; the significance in anisotropy in atomic bonding is reduced as the Goldschmidt radius ($R_{M(G)}$) of the M atom and thereby the c/a axial ratio of the AlB_2-type borides increases due to the occurrence of the elongation of the electronic charge around the M atom along the c-axis by an amount corresponding to the value of $R_{M(G)}$-$R_{M(ideal)}$. The values of c_{44}/c_{66} for MgB_2 and AlB_2 are exceptionally small. This may be because the bonding nature for metal diborides without *d* electrons is quite different from that for metal diborides with *d* electrons.

5. Conclusions

(1) All the five independent monocrystal elastic constants of CrB_2, TiB_2 and ZrB_2 have been determined in the temperature range from 300 to 1373K. The anisotropic parameters of c_{33}/c_{11}

and c_{44}/c_{66} as well as the ratios of the Young moduli and reciprocals of linear compressibilities along the *a*- and *c*-axes (E_c/E_a, $\beta_c^{-1}/\beta_a^{-1}$) are smaller than unity. These anisotropic parameters decrease in the order of ZrB_2, TiB_2 and CrB_2. The small values of Possion ratio (CrB_2: 0.207, TiB_2: 0.111, ZrB_2: 0.135 at 300 K) indicate the strong covalence in these diborides.

(2) The values of thermal expansivities along the *a*- and *c*-axes of CrB_2, TiB_2 and ZrB_2 have been determined in the temperature range from 300 to 1073K. The temperature dependence of the theramal expansivities along the *a*- and *c*-axes for CrB_2 is considerably large whereas that for TiB_2 and ZrB_2 is relatively small. The ratio of the theramal expansivities along the *a*- and *c*-axes (α_c/α_a) for TiB_2 is larger than that for ZrB_2.

(3) The ratio of the bond strength out of basal plane to that in basal plane increases in the order of CrB_2, TiB_2 and ZrB_2, as evidenced with the force constant ratio of k_a/k_c calculated by an approach similar to the valence-force-field method. The significance in anisotropy in atomic bonding in AlB_2-type diborides is reduced as the Goldschmidt radius ($R_{M(G)}$) of the M atom and thereby the *c*/*a* axial ratio of the AlB_2-type borides increases due to the occurrence of the elongation of the electronic charge around the M atom along the *c*-axis by an amount corresponding to the value of $R_{M(G)}$-$R_{M(ideal)}$.

Acknowledgments

This work was partly supported by the Global COE (Center of Excellence) Program of International Center for Integrated Research and Advanced Education in Materials Science from the Ministry of Education, Culture, Sports, Science and Technology (MEXT), Japan.

References

[1] Goldschmidt HJ. Interstitial Alloys. London: Butterworths, 1967. p.p.254-295.

[2] Casting J, Costa P. Properties and Uses of Diborides. In: Matkovich VI, editor. Boron and Refractory Borides. Berlin: Springer-Verlag, 1977. p.p.390-412.

[3] Brotherton RJ, Steinberg H. Progress in Boron Chemistry. New York: Pergamon, 1970. p.p.202-217.

[4] Kulikowski Z, Godfrey TMT, Wisbey A, Goodwin PS, Langlais F, Flower HM, Zheng JG, Davies DP. Mater Sci Technol 2000;16:1453.

[5] Pelleg J. J Vac Sci Technol B 2000;18:1338.

[6] Chen HK, Liu JR, Shen SJ, Huang WD. Rare Metal Mater Eng 2005;34:1921.

[7] Kinoshita H, Otani S, Kamiyama S, Amano H, Akasaki I, Suda J, Matsunami H. Jpn J Appl Phys 2001;40:L1280.

[8] Suda J, Matsunami H. J Cryst Growth 2002;237:1114.

[9] Hughes WC, Rowland WH, Johnson MAL, Fujita S, Cook JW, Schetzina JF, Ren J, Edmond JA. J Vac Sci Technol B 1995;13:1571.

[10] Okamoto NL, Kusakari M, Tanaka K, Inui H, Yamaguchi M, Otani S. J Appl Phys 2003;93:88.

[11] Okamoto NL, Kusakari M, Tanaka K, Inui H, Yamaguchi M, Otani S. Mater Res Soc Symp Proc 2003;753:83.

[12] Yamada-Takamura Y, Wang ZT, Fujikawa Y, Sakurai T, Xue QK, Tolle J, Liu PL, Chizmeshya AVG, Kouvetakis J, Tsong IST. Phys Rev Lett 2005;95:266105.

[13] Villars P. Pearson's Handbook: Crystallographic Data for Intermetallic Phases. Amsterdam: ASM International, 1997.

[14] Massalski TB. Binary Alloy Phase Diagram. Ohio: ASM, 1986. p.349.

[15] Post B, Glaser FW, Moskowitz D. Acta Metal 1954;2:20.

[16] McHale AE, McMurdie HF, Ondik HM. Phase Diagrams for Ceramists; Borides, Carbides, and Nitrides. Westerville, OH: American Ceramic Society, 1994. p.p.144-146.

[17] Otani S, Ishizawa Y. J Cryst Growth 1996;165:319.

[18] Otani S, Korsukova MM, Mitsuhashi T. J Cryst Growth 1998;186:582.

[19] Tanaka K, Koiwa M. High Temp Mater Proc 1999;18:323.

[20] Spoor PS, Maynard JD, Pan MJ, Green DJ, Hellmann JR, Tanaka T. Appl Phys Lett 1997;70:1959.

[21] Gilman JJ, Roberts BW. J Appl Phys 1961;32:1405.

[22] Nye JF. Physical Properties of Crystals. Oxford: Clarendon Press, 1992. p.p.144-146.

[23] Hill R. P Phys Soc Lond A 1952;65:349.

[24] Gshneidner KJ. Physical Properties and Interrelationships of Metallic and Semimetallic Elements. In: Seitz F, Turnbull D, editors. Solid State Physics, vol. 16. New York: Academic Press, 1964. p.308.

[25] Nishihara Y, Tokumoto M, Yamaguchi Y, Ogawa S. J Phys Soc Jpn 1987;56:1562.

[26] Decker BF, Kasper JS. Acta Crystallogr 1959;12:503.

[27] Pearson WB. Crystal Chemistry and Physics of Metals and Alloys. New York: Wiley, 1972. p.p.135-197.

[28] Tanaka K, Onome H, Inui H, Yamaguchi M, Koiwa M. Materials Science and Engineering a-Structural Materials Properties Microstructure and Processing 1997;240:188.

[29] Tanaka K, Inui H, Yamaguchi M, Koiwa M. Mater Sci Eng A 1999;261:158.

[30] Martin RM. Phys Rev B 1970;1:4005.

[31] Kim K, Lambrecht WRL, Segall B. Mater Res Soc Symp Proc 1996;395:399.

[32] When bond-bending terms are incorporated in the model, the number of independent

force constants becomes as many as six, which is larger than that of independent elastic constants (five) so that the force constants cannot be deduced from the experimentally determined elastic constants. We can consider six different bond-bending terms: M-M-M, B-B-B, B-M-B, M-B-M, M-M-B and B-B-M. The force constants in the first and second terms are linearly dependent, and so are those in the third and forth terms. However, the force constants in the fifth and sixth terms are linearly independent. Thus, the number of independent force constants for bond-bending terms is four, producing six in total including force constants for bond-stretching terms (two independent force constants as stated in the text).

[33] Shein IR, Ivanovskii AL. J Phys-Condens Mat 2008;20:415218.

Figure captions

Fig. 1. (Color online) (a) Crystal structure of metal diborides with the hexagonal AlB_2 structure. The frame indicates a unit cell. Projection of the crystal structure along the (b) [0001] and (c) $[11\bar{2}0]$ directions.

Fig. 2. Experimental lattice constants of various metal diborides with the AlB_2 structure. Data are taken after Ref. 13.

Fig. 3. (Color online) Five independent monocrystal elastic constants of (a) CrB_2, (b) TiB_2 and (c) ZrB_2 plotted as a function of temperature. Experimental error bars are smaller than the symbol sizes.

Fig. 4. (Color online) Orientation dependence of Young modulus at 300 and 1373 K on $(1\bar{1}00)$ prism plane for CrB_2, TiB_2 and ZrB_2.

Fig. 5. (Color online) Young, bulk, shear moduli and Poisson ratio for polycrystals of (a) CrB_2, (b) TiB_2 and (c) ZrB_2 plotted as a function of temperature. Experimental error bars for moduli are smaller than the symbol sizes.

Fig. 6. (Color online) Thermal expansivities for (a) CrB_2, (b) TiB_2 and (c) ZrB_2 along the *a*- and *c*-axes plotted as a function of temperature.

Fig. 7. (Color online) Anisotropic parameters in elasticity, c_{33}/c_{11}, c_{44}/c_{66}, E_c/E_a and $\beta_c^{-1}/\beta_a^{-1}$ for CrB_2, TiB_2 and ZrB_2 as well as those in thermal expansivities, α_c/α_a, plotted as a function of the magnitude of their *a*-axis lattice constant. Experimental error bars are smaller than the symbol sizes.

Fig. 8. (Color online) Schematics of the distribution of the electronic charge around M atoms in the $(0\bar{1}10)$ plane. The value of $R_{M(G)} - R_{M(ideal)}$ is (a,b) positive and (c,d) negative. (a,c) Uniform and (b,d) non-uniform distributions of the electronic charge around the M atoms are assumed.

Fig. 9. Anisotropic parameters of c_{44}/c_{66} for several metal diborides derived by ab-initio

calculations [33] (open circles) and those for CrB_2, TiB_2 and ZrB_2 experimentally determined in the present study (solid circles) plotted as a function of the value of $R_{M(G)} - R_{M(ideal)}$. Experimental error bars are smaller than the symbol sizes.

Table 1. Lattice constants, *c*/*a* axial ratio, B-B atomic distance, melting temperature, Goldschmidt radius of the constituent metal atom, $R_{M(G)}$, and the difference between the Goldschmidt radius of the metal atom and the ideal one ($R_{M(ideal)}$) for CrB_2, TiB_2, ZrB_2, and the ideal diboride.

	a (nm)	*c* (nm)	*c*/*a*	B-B (nm)	T_m (K)	$R_{M(G)}$ (nm)	$R_{M(G)}$-$R_{M(ideal)}$ (nm)
CrB_2	0.2973[a]	0.3072[a]	1.033	0.1716	2473[b]	0.128[f]	-0.024
TiB_2	0.3038[a]	0.3239[a]	1.066	0.1754	3193[c]	0.146[f]	-0.006
ZrB_2	0.3130[a]	0.3533[a]	1.129	0.1807	3518[d]	0.160[f]	+0.008
Ideal	0.305	0.328	1.0746	0.176[e]	-	0.152	0

[a] Ref. 13.
[b] Ref. 14.
[c] Ref. 15.
[d] Ref. 16.
[e] Ref. 26.
[f] Ref. 27.

Table 2. Dimensions of specimens used for the measurements of elastic constants and thermal expansivities.

Dimensions (mm)		CrB_2	TiB_2	ZrB_2
Elastic constants	[0001]	2.819	2.395	3.762
	$[11\bar{2}0]$	2.792	3.752	3.673
	$[1\bar{1}00]$	2.452	2.788	3.694
Thermal expansivities (longitudinal axis)	*a*-axis	6.142	6.245	6.862
	c-axis	8.709	7.244	7.910

Table 3. Monocrystal elastic constants at 300 K in the form of $c_{ij} = c_{ij(300K)} + k(T - 300)$ where $c_{ij(300K)}$, k and T stand for the elastic constant at 300 K, numerical constant and temperature in Kelvin, respectively, and anisotropic parameters (c_{33}/c_{11} and c_{44}/c_{66}) at 300 K. The numerical constants are shown in the parentheses. Previously reported monocrystal elastic constants for TiB_2 are also tabulated for comparison [20, 21].

	c_{11} (GPa)	c_{33} (GPa)	c_{12} (GPa)	c_{13} (GPa)	c_{44} (GPa)	c_{66}* (GPa)	c_{33}/c_{11}	c_{44}/c_{66}
CrB_2	583.7 (-0.0586)	343.3 (-0.0311)	117.3 (0.0044)	119.7 (-0.0044)	143.1 (-0.0284)	233.2 (-0.0315)	0.588	0.614
TiB_2	654.5 (-0.0412)	454.5 (-0.0305)	56.5 (0.0060)	98.4 (-0.0016)	263.2 (-0.0253)	299.0 (-0.0236)	0.694	0.880
TiB_2[a]	660	432	48	93	260	306	0.655	0.850
TiB_2[b]	690	440	410	320	250	140	0.638	1.786
ZrB_2	567.8 (-0.0431)	436.0 (-0.0294)	56.9 (0.0051)	120.5 (-0.0022)	247.5 (-0.0261)	255.4 (-0.0241)	0.768	0.969

* $c_{66}=(c_{11} - c_{12})/2$
[a] Ref. 20.
[b] Ref. 21.

Table 4. Values of Young moduli and reciprocals of linear compressibilities along the *a*- and *c*-axes at 300 K.

	Young moduli			Reciprocals of linear compressibilities		
	E_a (GPa)	E_c (GPa)	E_c/E_a	β_a^{-1} (GPa)	β_c^{-1} (GPa)	$\beta_c^{-1}/\beta_a^{-1}$
CrB_2	531.4	302.4	0.569	948.2	459.3	0.484
TiB_2	631.2	427.2	0.677	853.1	590.8	0.692
ZrB_2	533.3	387.7	0.727	772.1	631.3	0.818

Table 5. Values of polycrystalline elastic moduli (Young (*E*), bulk (*B*), shear (*G*)) and Poisson ratio (ν) at 300 K obtained by linear fitting with Eq. (1). The numerical constants obtained by linear fitting are shown in the parentheses.

	E (GPa)	*B* (GPa)	*G* (GPa)	ν
CrB_2	422.5 (-0.0594)	240.2 (-0.0170)	175.0 (-0.0273)	0.206 (2.21×10^{-5})
TiB_2	583.5 (-0.0450)	250.0 (-0.0125)	262.6 (-0.0226)	0.111 (1.10×10^{-5})
ZrB_2	526.0 (-0.0457)	240.1 (-0.0127)	231.7 (-0.0225)	0.135 (1.32×10^{-5})

Table 6. Values of thermal expansivities averaged over the temperature range from 300 to 1073 K and the ratio of the thermal expansivities along the *a*- and *c*-axes.

	α_a ($\times 10^{-6}$ [K^{-1}])	α_c ($\times 10^{-6}$ [K^{-1}])	α_c / α_a
CrB_2	9.66	8.81	0.91
TiB_2	6.35	9.30	1.46
ZrB_2	6.66	6.93	1.04

Table 7. Values of the coefficients of the second term in Eqs. (9) and (10) and the ratio of k_a/k_c with which the value of c_{44}/c_{66} coincides with the experimentally determined value.

	c_{44}	c_{66}	k_a/k_c
CrB_2	2.963	0.925	1.30
TiB_2	2.981	0.874	0.84
ZrB_2	2.998	0.784	0.77

Figure 1

Click here to download high resolution image

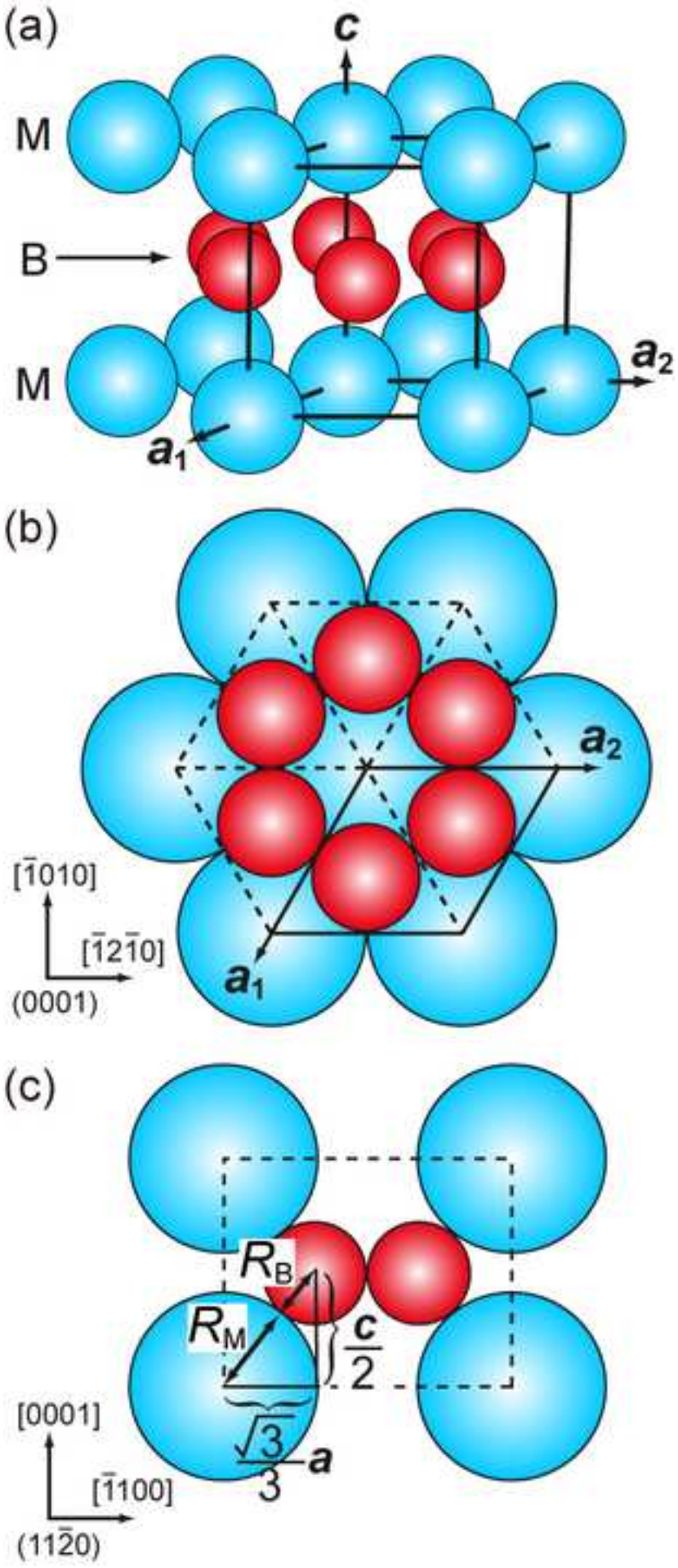

Figure 2

Click here to download high resolution image

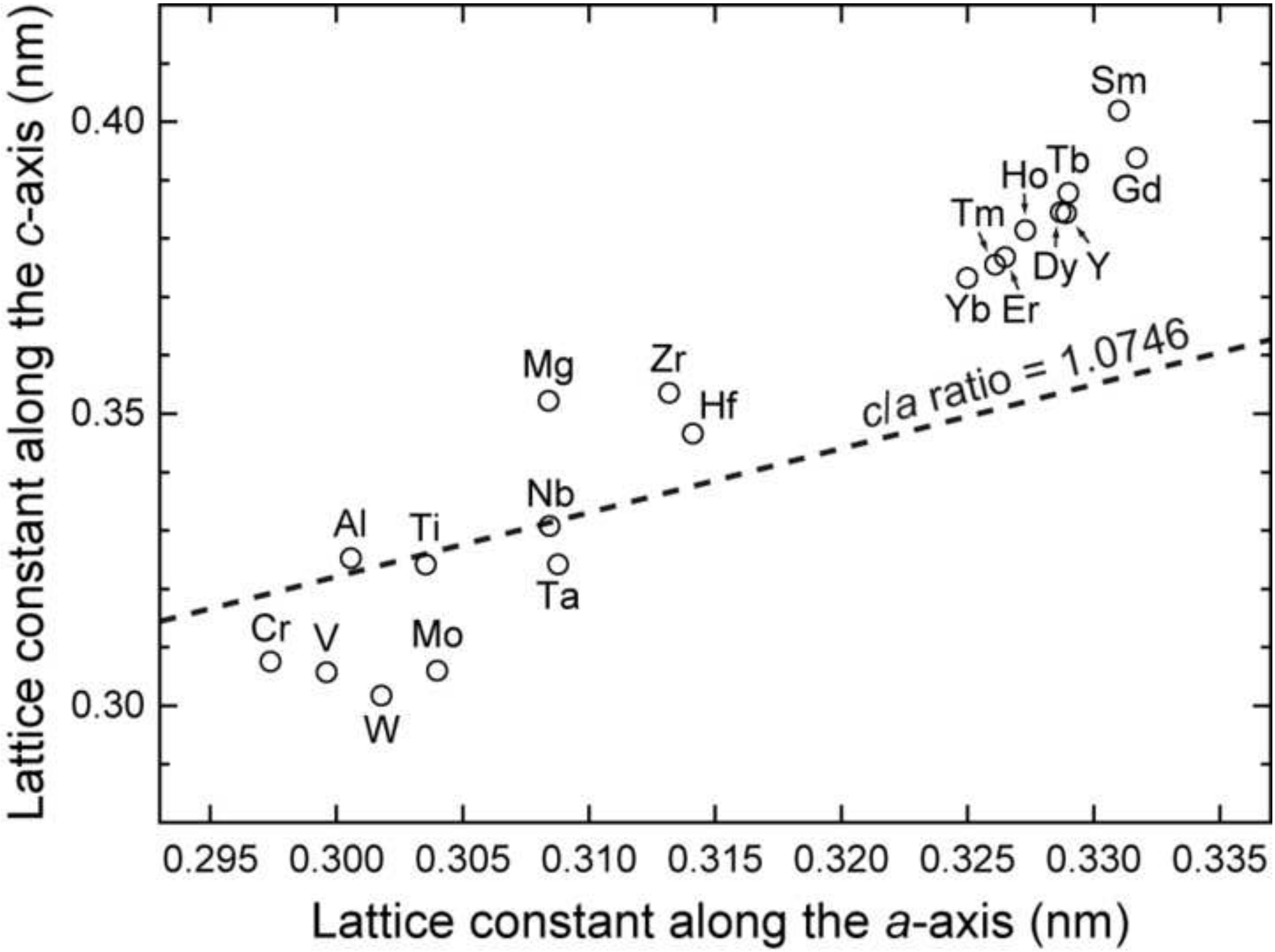

Figure 3

Click here to download high resolution image

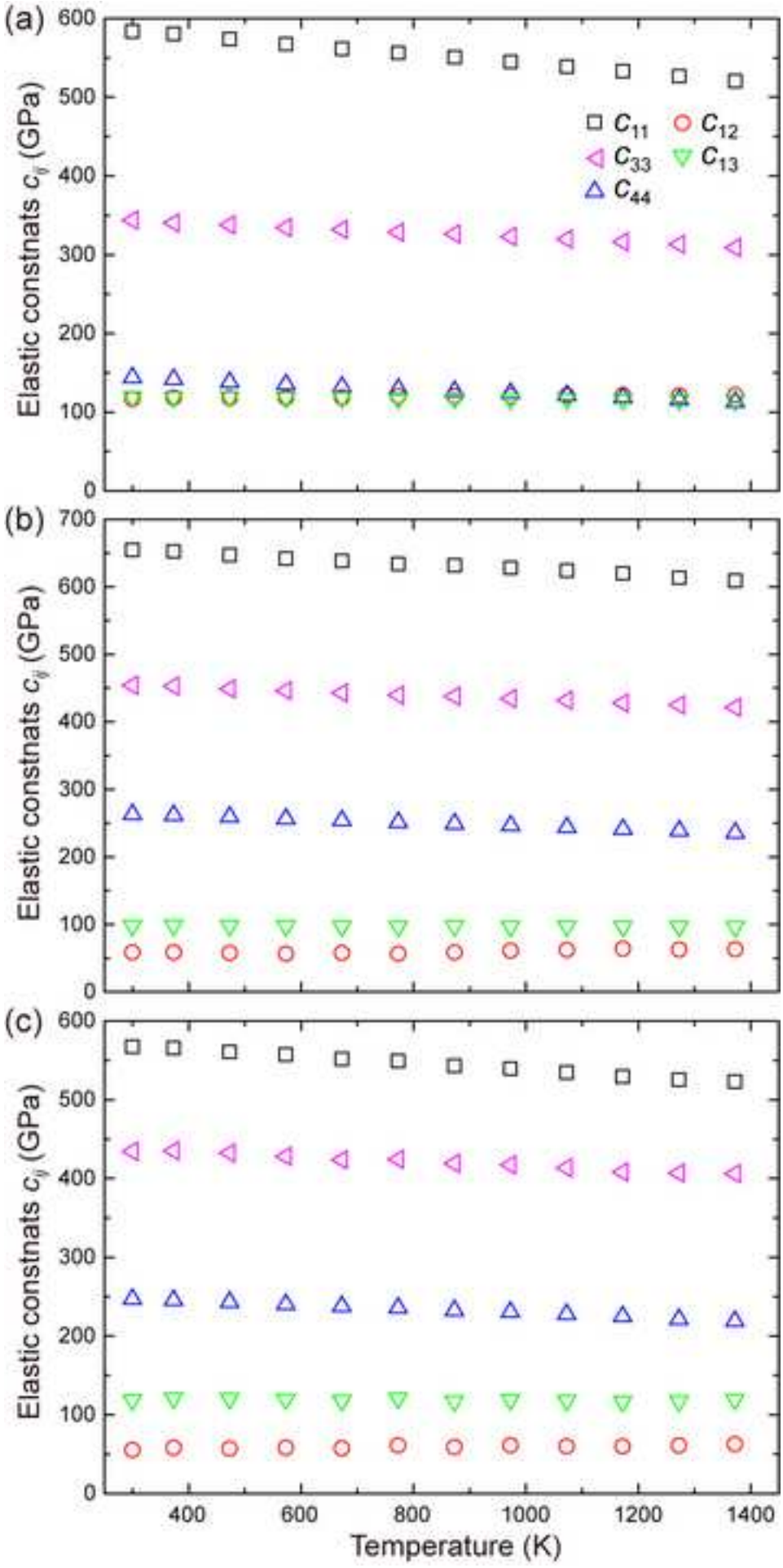

Figure 4

Click here to download high resolution image

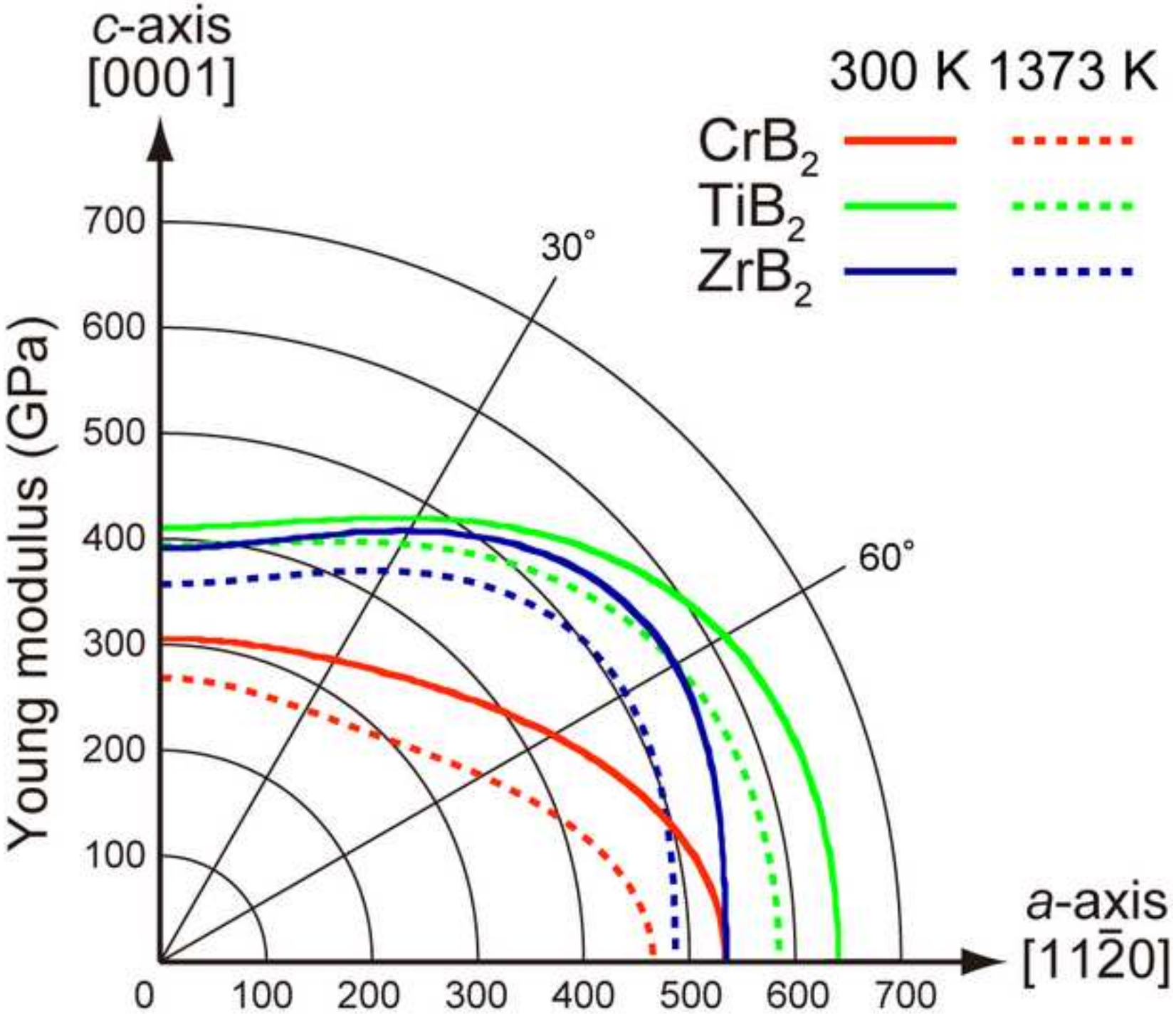

Figure 5

Click here to download high resolution image

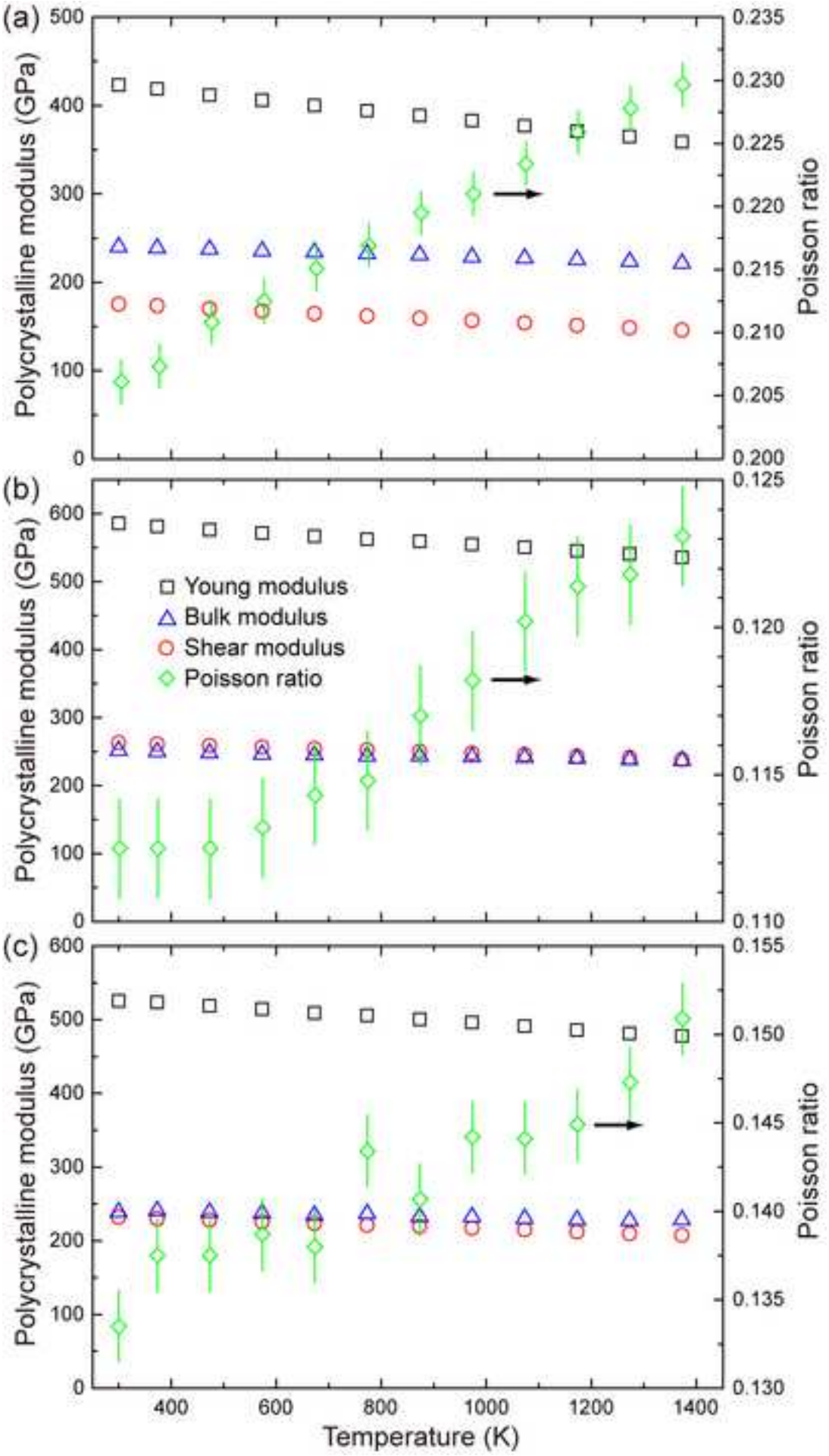

Figure 6

Click here to download high resolution image

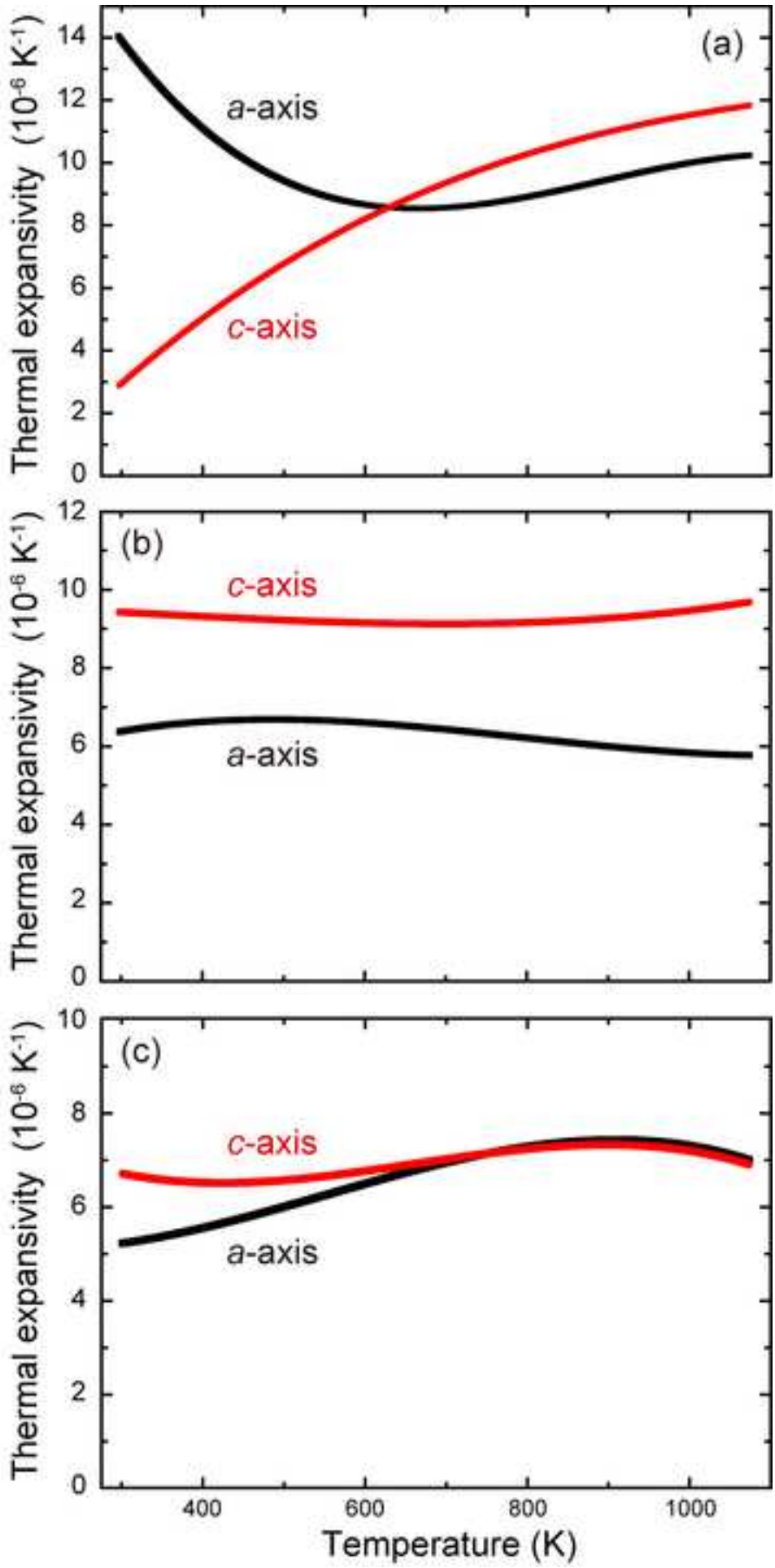

Figure 7

Click here to download high resolution image

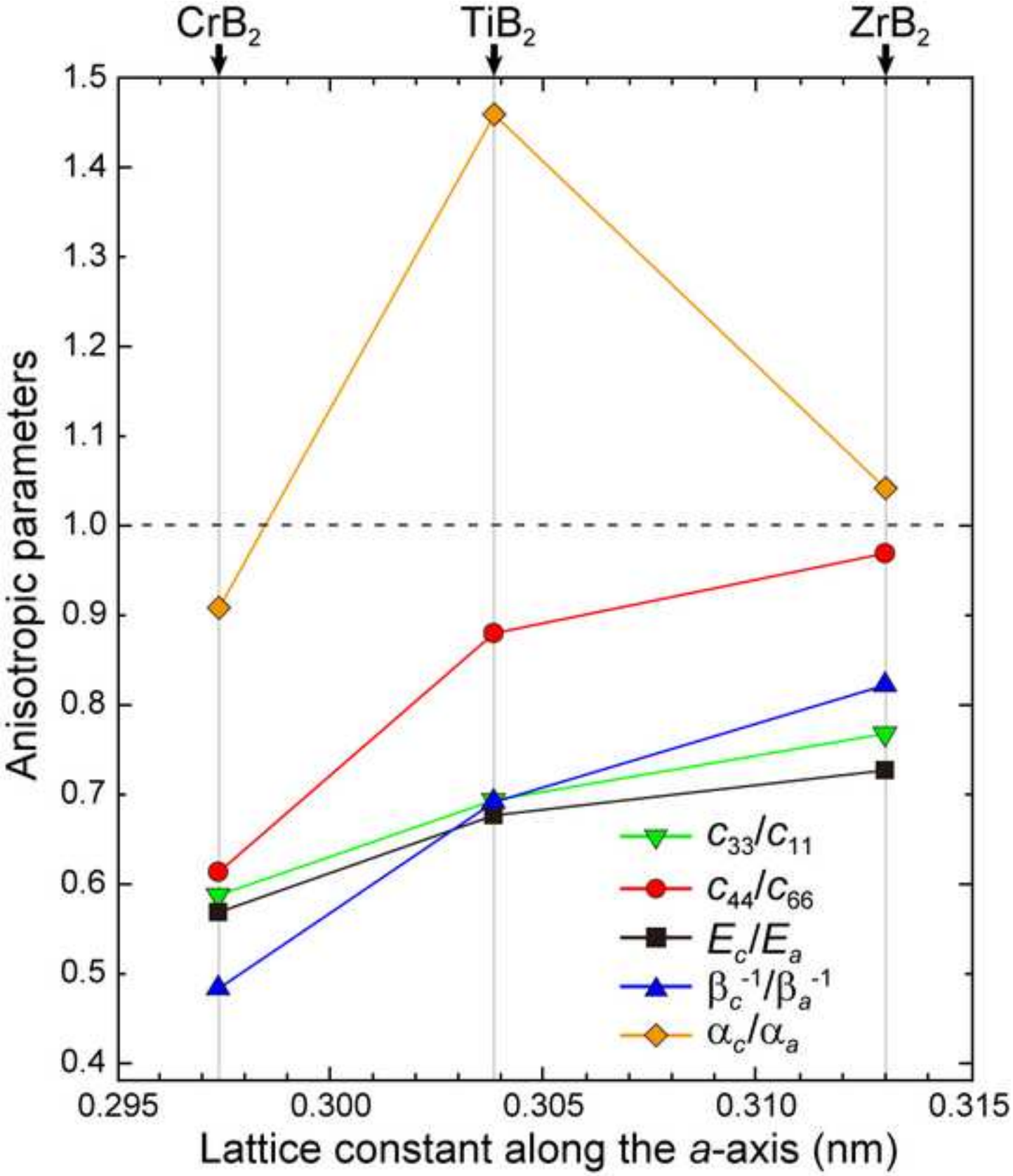

Figure 8

Click here to download high resolution image

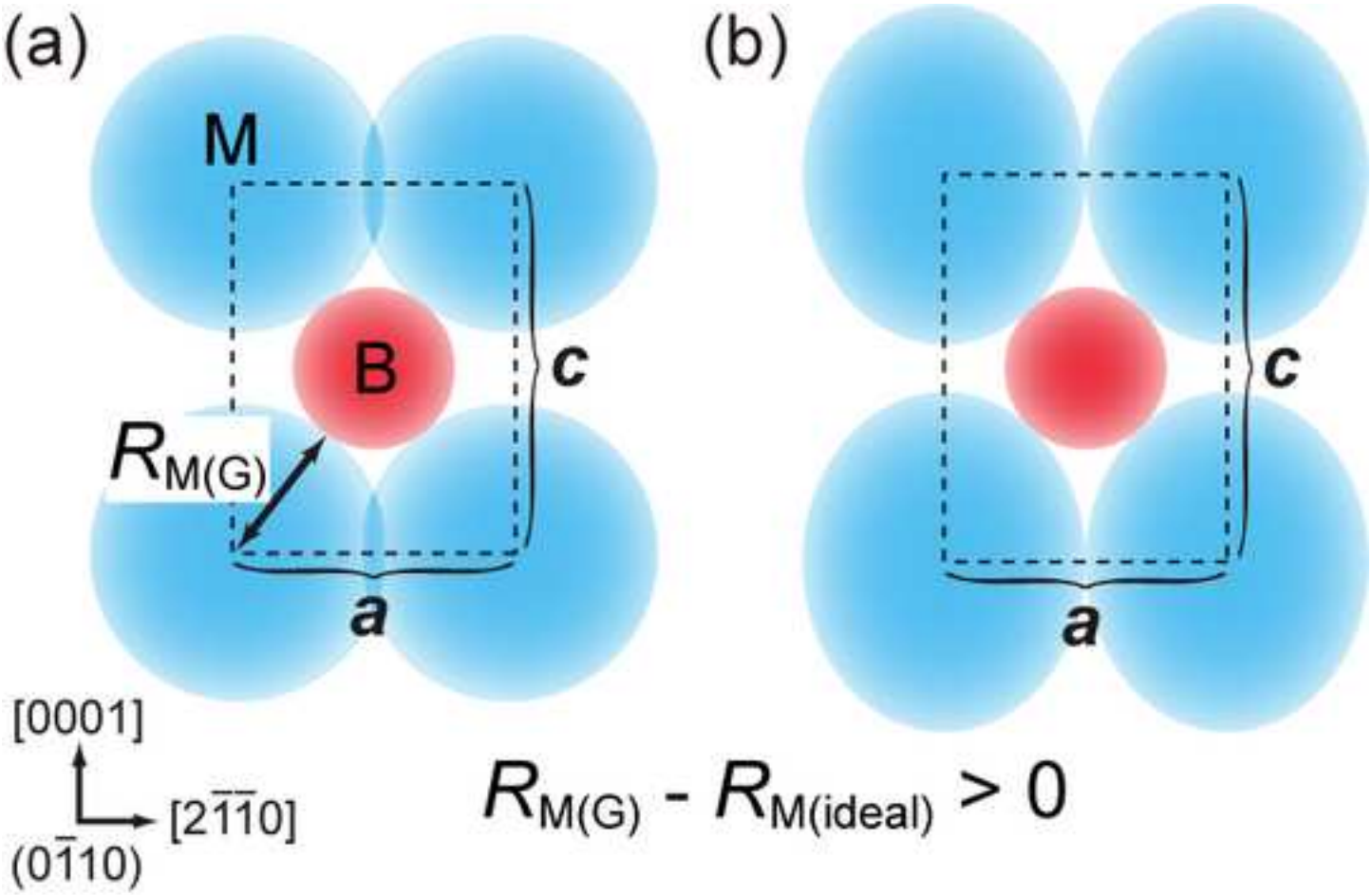

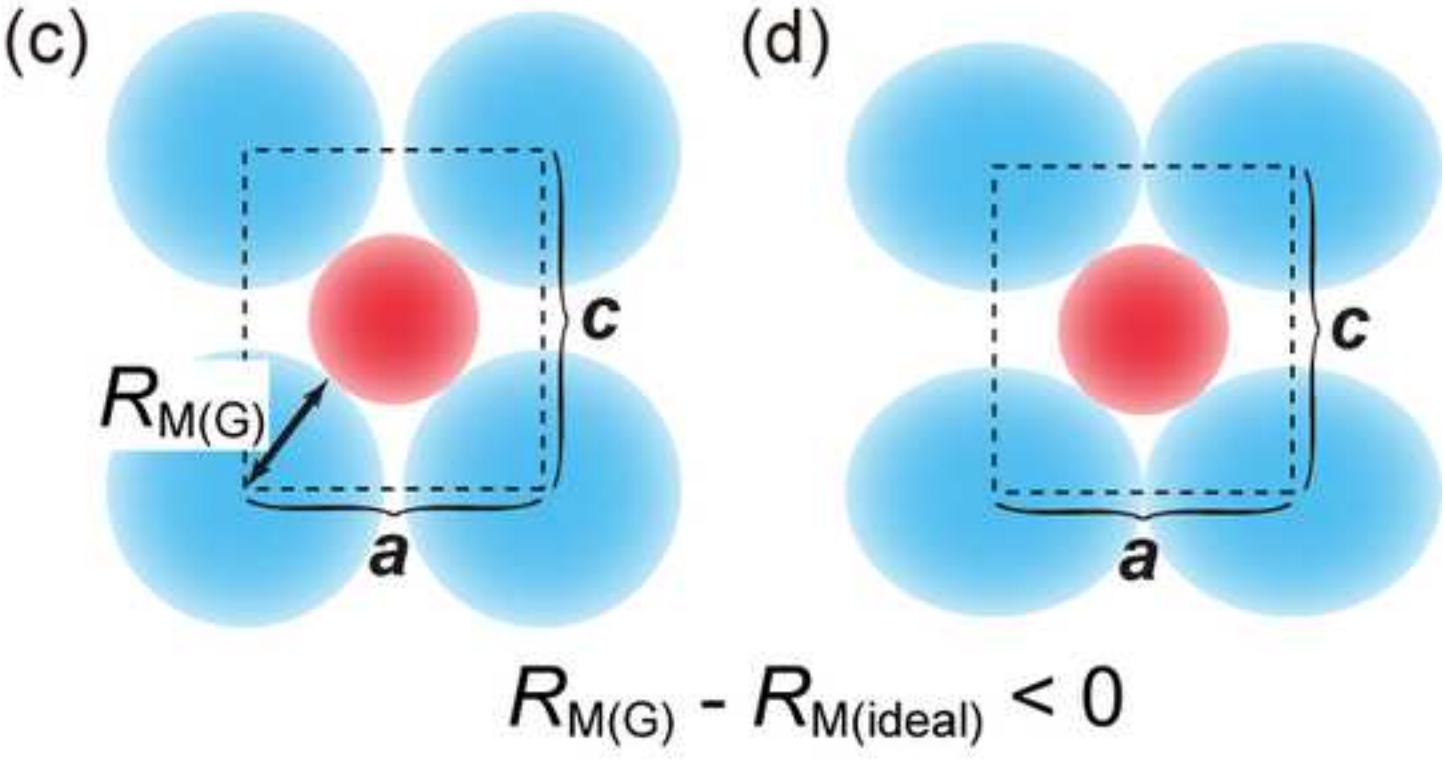

Figure 9

Click here to download high resolution image